

Efficient angle-domain common-image gathers using Cauchy-condition-based polarization vectors

Xiongwen Wang¹, Jianliang Qian², and Huazhong Wang³

Right Running Head: Angle-domain common-image gathers

¹ School of Ocean and Earth Science, Tongji University, Shanghai, 200092. Email:

xiongwenwang@icloud.com

² Department of Mathematics, Michigan State University, East Lansing, MI 48824. Email:

qian@math.msu.edu

³ School of Ocean and Earth Science, Tongji University, Shanghai, 200092. Email:

herbhuak@vip.163.com

ABSTRACT

Because angle-domain common-image gathers (ADCIGs) from reverse-time migration are capable of obtaining correct illumination of subsurface geological structure, ADCIGs provide more reliable information for velocity model building, amplitude-variation versus angle analysis, and attribute interpretation. The approaches for generating ADCIGs mainly consist of two types: indirect approaches convert extended image gathers into ADCIGs while direct approaches first obtain propagating angles of wavefronts and then map the imaging result to the angle domain. In practice, however, generation of ADCIGs usually incurs high computational cost, poor resolution and other drawbacks. In order to generate efficient ADCIGs by using reverse-time migration methods, we propose a novel approach to obtain polarization vectors – directions of particle motion – from the Cauchy wavefield (CWF) and an efficient localized plane-wave decomposition algorithm to implement the angle-domain imaging condition. The CWF is a wavefield constructed from the Cauchy condition of the wave equation at any given time, and it only contains negative frequencies of the original wavefield so that the polarization vector is obtained from the local CWF in the wavenumber domain. With polarization vectors at our disposal, we further propose an efficient localized plane-wave decomposition algorithm to implement the angle-domain imaging condition. Numerical examples show that the new approach is able to handle complex wave phenomenon and has advantages in illuminating subsurface structure.

INTRODUCTION

Common-image gathers (CIGs) are collections of migrated traces sharing a common-surface (or common-subsurface) location or a common-scattering angle, and they provide crucial information for velocity model building, amplitude-variation versus angle analysis (AVA), and attribute interpretation and bridge the gap between seismic imaging and reservoir characterization. Offset-domain common-image gathers (ODCIGs) indexed by the surface offset in migrations of Kirchhoff type suffer from kinematic artifacts (Xu et al., 2001; Stolk and Symes, 2004), while angle-domain common-image gathers (ADCIGs) indexed by the subsurface incident angle in wave-equation migration reduce the artifacts and provide more reliable information of subsurface (Sava and Fomel, 2003; Biondi and Symes, 2004; Stolk and Symes, 2004). Therefore, ADCIGs are more powerful for obtaining illumination information in places where geological structure is complex.

Many methods are proposed to obtain ADCIGs in the literature. These methods can be roughly divided into two types: indirect and direct approaches. The indirect approaches first obtain extended image gathers generated by extended imaging conditions and then convert these gathers to ADCIGs in that these methods do not compute the incident angle directly when applying the imaging condition (Sava and Fomel, 2003; Fomel, 2004; Sava and Fomel, 2006). Extended image gathers used in the indirect approaches for ADCIGs include subsurface-offset CIGs and time-delay CIGs. Sava and Fomel (2003) proposed an approach to converting subsurface-offset CIGs of one-way wave-equation migration (OWEM) into ADCIGs; see also De Bruin et al. (1990). The conversion between subsurface-offset CIGs

and ADCIGs is efficient for two dimensions, but is very expensive for three dimensions (Fomel, 2004). In order to reduce the cost of conversion between two different imaging domains for three dimensions, Sava and Fomel (2006) proposed another approach to converting time-delay CIGs into ADCIGs; however, the conversion between time-delay CIGs and ADCIGs is only feasible for narrow-azimuth data and suffers from sampling issues which degrades the quality of the resulting ADCIGs (Xu et al., 2011).

The direct approaches are based on the Poynting vector or local plane-wave decomposition. The approaches based on the Poynting vector first compute the propagating angle of wavefronts defined by the Poynting vector and then map the imaging result to the angle domain (Yoon and Marfurt, 2006; Vyas et al., 2011; Dickens and Winbow, 2011; Yoon et al., 2011). Since the Poynting vector actually indicates the polarization of energy flow, it is not the polarization vector of particle motion when wavefronts self-intersect. Moreover, the Poynting vector is unstable when the wavefield contains noise, which hinders the application of the Poynting vector in computing propagating angles of receiver wavefields. ADCIGs are also generated directly from one-way wave-equation migrations or reverse-time migrations. Since the wavefields obtained by one-way wave equations only contain down-going or up-going waves with propagating angles ranging from 0 to 180 degrees, it is convenient to produce ADCIGs from OWEM algorithms by decomposing wavefields into a sequence of local plane waves (Xie and Wu, 2002; Soubaras, 2003; Wu et al., 2004). However, the OWEM algorithm limits the imaging angle and does not retain the true-amplitude information (Zhang et al., 2003), which further hinders its application in the AVA analysis. Therefore, alternative approaches were proposed to decompose the full wavefields into local plane waves

(Xie and Yang, 2008; Cao and Wu, 2009). Xu et al. (2011) proposed a reverse-time migration (RTM) based approach to obtain ADCIGs. This approach first Fourier-transforms wavefields from the time domain to the frequency domain and then implements local plane-wave decomposition in the wavenumber domain, where an anti-leakage Fourier-transform (ALFT) algorithm (Xu et al., 2005, 2010) is used in the local plane-wave decomposition to reduce computational cost and Gibbs phenomenon. Since time-sliced wavefields are generated by solving underlying time-domain wave equations and are recorded by using the time direction as the evolution direction (the slowest dimension in computer storage), it is necessary to transpose the recorded wavefields to make the time direction the fastest direction. This transpose in time increases the input/output cost and limits the usage of RTM. To retain the accuracy of RTM and improve efficiency of existing ADCIGs, we propose a new approach to obtain polarization vectors – directions of particle motion – by using the Cauchy condition.

Because the solution of a pure initial-value wave equation is uniquely determined by the Cauchy condition when there is no external force, the Cauchy condition yields the information of polarization vectors. According to this observation, we propose a novel approach to construct a complex-valued wavefield containing only negative frequencies from two real-valued Cauchy conditions defined by the instantaneous displacement and velocity, and we name this complex-valued wavefield the Cauchy wavefield (CWF). The construction of CWFs was first proposed by the authors in Wang et al. (2015), and we further systematically develop this approach in the current paper. Since a CWF contains only negative frequencies, the energy distribution of a CWF in the wavenumber domain reveals the in-

formation of polarization vectors: the positivity of the i -th component of the wavenumber vector indicates that the wave travels along the positive direction of the i -th spatial coordinate. This unique feature allows us to carry out the local plane-wave decomposition in the time domain conveniently without transforming the whole time-domain wavefield into the frequency-domain wavefield so that the imaging condition is realized efficiently and the imaging result is mapped to the angle domain directly. Since it is implemented directly in the process of modeling wavefields, the proposed CWF approach is applicable to all kinds of RTM algorithms. In order to reduce computational cost of zero-lag cross-correlation imaging conditions, we also propose an imaging condition using only significant local plane waves. Finally, we show some numerical examples of ADCIGs to demonstrate the performance of the new method.

The rest of the paper is organized as follows. First, we present the formulation of CWFs and prove that a CWF contains only negative frequencies. Second, we present an efficient method to carry out local plane-wave decomposition. With CWFs and decomposed local plane-waves at our disposal, we present the imaging condition in the angle domain. ADCIGs of a layered model and the Marmousi model demonstrate the performance of our methods.

CONSTRUCTION OF THE CAUCHY WAVEFIELD

Consider the pure initial-value wave equation

$$\begin{cases} \left(\Delta - \frac{1}{v^2(\mathbf{x})} \frac{\partial^2}{\partial t^2} \right) u(\mathbf{x}, t) = 0, & \mathbf{x} \in \mathbf{R}^d, \quad t > 0, \\ u(\mathbf{x}, t)|_{t=t_0} = f_1(\mathbf{x}) \\ \partial_t u(\mathbf{x}, t)|_{t=t_0} = f_2(\mathbf{x}) \end{cases} \quad (1)$$

where $d = 2$ or 3 , $\mathbf{x} = (x, z)$ for $d = 2$ or $\mathbf{x} = (x, y, z)$ for $d = 3$, $v(\mathbf{x})$ is the sound speed, and $f_1(\mathbf{x})$ and $f_2(\mathbf{x})$ are real-valued square-integrable functions. Since the solution of this equation is uniquely determined by the initial condition (the Cauchy condition), the Cauchy condition contains information of directions of particle motion, the so-called polarization vectors. Although seismic records or wavefields are real-valued, we assume that the solution for the wave equation takes the following asymptotic form so as to simplify formulations:

$$u(\mathbf{x}, t) = A(\mathbf{x}, t) e^{i\phi(\mathbf{x}, t)} \quad (2)$$

where $A(\mathbf{x}, t)$ and $\phi(\mathbf{x}, t)$ denote the amplitude and phase of the wavefield, respectively.

Differentiating (2) with respect to time t , we have

$$u_t(\mathbf{x}, t) = (A_t(\mathbf{x}, t) + iA(\mathbf{x}, t) \phi_t(\mathbf{x}, t)) e^{i\phi(\mathbf{x}, t)}. \quad (3)$$

In the high-frequency regime, u_t is approximated by

$$\begin{aligned} u_t(\mathbf{x}, t) &\approx iA(\mathbf{x}, t)\phi_t(\mathbf{x}, t)e^{i\phi(\mathbf{x}, t)} \\ &= i\omega(\mathbf{x}, t)u(\mathbf{x}, t) \end{aligned} \tag{4}$$

where A_t is much smaller than $A\phi_t$ in magnitude and is thus neglected (this assumption is also correct for low frequencies because the amplitude of low frequencies varies slowly), and $\omega(\mathbf{x}, t)$ is the instantaneous frequency of $u(\mathbf{x}, t)$. According to the dispersion relation, $\omega(\mathbf{x}, t)$ satisfies the following equation:

$$\begin{aligned} \omega^2(\mathbf{x}, t) &= v^2(\mathbf{x})|\mathbf{k}(\mathbf{x}, t)|_2^2 \\ \Rightarrow |\omega(\mathbf{x}, t)| &= v(\mathbf{x})|\mathbf{k}(\mathbf{x}, t)| \end{aligned} \tag{5}$$

where $\mathbf{k}(\mathbf{x}, t)$ is the instantaneous wavenumber of u and is defined by

$$\mathbf{k}(\mathbf{x}, t) = \nabla\phi(\mathbf{x}, t). \tag{6}$$

Using equations (4), (5), and (6), we construct a complex-valued wavefield, named the Cauchy wavefield as it is based on the instantaneous Cauchy condition, by the following

formula:

$$\begin{aligned}
c(\mathbf{x}, t) &= \frac{1}{2} \left(u(\mathbf{x}, t) + i \frac{u_t(\mathbf{x}, t)}{v(\mathbf{x}) |\nabla \phi(\mathbf{x}, t)|} \right) \\
&\approx \frac{1}{2} \left(u(\mathbf{x}, t) - \frac{\omega(\mathbf{x}, t) u(\mathbf{x}, t)}{v(\mathbf{x}) |\mathbf{k}(\mathbf{x}, t)|} \right) \\
&= \frac{1}{2} (1 - \text{sgn}(\omega)) u(\mathbf{x}, t) \\
&= \frac{1}{2\pi} \int_{-\infty}^0 \tilde{u}(\mathbf{x}, \omega) e^{i\omega t} d\omega, \tag{7} \\
\text{sgn}(\omega) &= \begin{cases} 1, & \omega > 0 \\ 0, & \omega = 0 \\ -1, & \omega < 0 \end{cases}
\end{aligned}$$

where $\tilde{u}(\mathbf{x}, \omega)$ is the Fourier transform of $u(\mathbf{x}, t)$ with respect to t . Equation (7) defines the CWF since it is constructed from the Cauchy condition of the wave equation (1). Note that $c(\mathbf{x}, t)$ only contains negative frequencies of $u(\mathbf{x}, t)$. Letting $\tilde{c}(\mathbf{k}, t)$ be the Fourier transform of $c(\mathbf{x}, t)$, we may use the direction of the wavenumber vector \mathbf{k} to determine the local propagation direction of waves: $k_x > 0$ indicates wave propagating in the positive direction of the x -coordinate while $k_x < 0$ indicates wave propagating in the negative direction of the x -coordinate; moreover, the amplitude spectrum of $\tilde{c}(\mathbf{k}, t)$ yields the distribution of wave vectors. Therefore, the energy distribution of local CWFs in the wavenumber domain reveals information of polarization vectors and can be used to carry out local plane-wave decompositions.

To compute CWFs rapidly, we observe that the imaginary part of the CWF can be obtained by the following relation: if $u_t(\mathbf{x}, t)$ is considered as a stationary signal, then

$$\text{Im}(c(\mathbf{x}, t)) = \frac{1}{2} F^{-1} \left(|\mathbf{k}|^{-1} F(u_t(\mathbf{x}, t) v^{-1}(\mathbf{x})) \right) \tag{8}$$

where F and F^{-1} are the forward and inverse Fourier transform with respect to \mathbf{x} and \mathbf{k} , respectively. Consequently, the CWF is constructed according to the following time-space equation

$$c(\mathbf{x}, t) = \frac{1}{2} \left(u(\mathbf{x}, t) + iF^{-1} \left(|\mathbf{k}|^{-1} F \left(u_t(\mathbf{x}, t) v^{-1}(\mathbf{x}) \right) \right) \right), \quad (9)$$

or the following time-wavenumber equation

$$\tilde{c}(\mathbf{k}, t) = F(c(\mathbf{x}, t)) = \frac{1}{2} \left(F(u(\mathbf{x}, t)) + i|\mathbf{k}|^{-1} F(u_t(\mathbf{x}, t) v^{-1}(\mathbf{x})) \right) \quad (10)$$

so that it can be computed rapidly and efficiently during wavefield modeling when the imaging condition is realized. Since this CWF construction formula only involves two additional Fourier transforms and the underlying RTM algorithms stay the same, we will use the CWF formula throughout this work.

LOCAL PLANE-WAVE DECOMPOSITION

Since a CWF contains only negative frequencies of $u(\mathbf{x}, t)$, the energy distribution of the CWF in the wavenumber domain reveals information of polarization vectors. In order to obtain ADCIGs, it is necessary to decompose CWFs into local plane waves so that the cross-correlation imaging condition is applied to these migrated local plane waves and the imaging result is mapped to the angle domain. Since the imaging condition is realized in the inner-most loop of an imaging algorithm, the corresponding computational cost is mainly determined by the efficiency of local plane-wave decomposition and the number of local

plane waves to be migrated. In order to have efficient local plane-wave decomposition and reduce the number of local plane waves, we will carry out the local plane-wave decomposition in a local space window at each imaging point and use only significant local plane waves to implement the imaging condition. A local space window is helpful to reduce the number of events in the considered local wavefield. Moreover, the wavefield in a local space window tends to be better approximated by superposition of local plane waves so that the number of local plane waves is dramatically reduced when the imaging condition is applied in a local space window. To have an efficient local plane-wave decomposition algorithm in realizing the imaging condition, we first project the energy distribution of a local CWF to a directional energy-distribution function, and we then solve an optimization problem to determine significant local plane-wave directions.

To simplify the presentation, we only discuss the local plane-wave decomposition of wavefields in 2-D cases, and a similar strategy applies to wavefields in 3-D cases. In order to decompose a local wavefield into local plane waves, the energy distribution of a local CWF in the wavenumber domain is first projected to each propagating angle according to the following relations:

$$\begin{aligned}
\beta(\mathbf{k}) &= \begin{cases} \gamma, & k_z \leq 0, \\ 2\pi - \gamma, & k_z > 0, \end{cases} & \gamma = \arccos(k_x/|\mathbf{k}|) \\
\Delta\alpha(\mathbf{k}) &= \arcsin\left(\frac{|\mathrm{d}\mathbf{k}|}{|\mathbf{k}|}\right) = \arcsin(1/(X|\mathbf{k}|)) \\
e(\theta) &= \sum_{|\theta - \beta(\mathbf{k})| < \Delta\alpha(\mathbf{k})} \left(1 - \frac{|\theta - \beta(\mathbf{k})|}{\Delta\alpha(\mathbf{k})}\right) |\tilde{c}(\mathbf{k}, t)|
\end{aligned} \tag{11}$$

where $\beta(\mathbf{k})$ defines the propagating angle of \mathbf{k} which ranges from 0 to 2π , $\Delta\alpha(\mathbf{k})$ defines the angle resolution of \mathbf{k} , X defines the aperture of the local space window in the x -direction, $\tilde{c}(\mathbf{k}, t)$ denotes the local CWF in the wavenumber domain, and $e(\theta)$ defines the energy of the local plane waves propagating in the direction θ . Equations in relation (11) project the energy of a local CWF to the angle domain, and the angle resolution of the directional energy-distribution function $e(\theta)$ is mainly determined by the aperture X of the local space window. Therefore, the local plane-wave decomposition is accomplished according to the energy-distribution function $e(\theta)$ in the following way:

$$\begin{aligned}
W &= \left\{ \theta \mid \partial_\theta e(\theta) = 0, \quad \partial_\theta^2 e(\theta) < 0 \right\}, \\
\bar{u}(\theta, \mathbf{k}, t) &= \begin{cases} \left(1 - \frac{|\theta - \beta(\mathbf{k})|}{\Delta\alpha(\mathbf{k})}\right) \tilde{c}(\mathbf{k}, t), & |\theta - \beta(\mathbf{k})| < \Delta\alpha(\mathbf{k}), \\ 0, & \text{else,} \end{cases} \quad (12) \\
\hat{u}(\theta, \mathbf{x}, t) &= \text{Re}(c(\theta, \mathbf{x}, t)) = \text{Re}\left(\int \bar{u}(\theta, \mathbf{k}, t) e^{i2\pi\mathbf{k}\cdot\mathbf{x}} d\mathbf{k}\right), \quad \theta \in W,
\end{aligned}$$

where W denotes the set defined by local maxima of $e(\theta)$, $\bar{u}(\theta, \mathbf{k}, t)$ denotes the local plane waves in the wavenumber domain propagating in the direction θ , the local plane wave $c(\theta, \mathbf{x}, t)$ in the time-space domain is obtained from the the inverse Fourier transform of $\bar{u}(\theta, \mathbf{k}, t)$, and $\hat{u}(\theta, \mathbf{x}, t)$ is the real part of $c(\theta, \mathbf{x}, t)$. Since $\hat{u}(\theta, \mathbf{x}, t)$ yields the desired local plane-wave decomposition of the original wavefield $u(\mathbf{x}, t)$, we will use equation (12) to carry out local plane-wave decomposition. In equation (12), W gives the possible propagating directions of local plane waves while $\bar{u}(\theta, \mathbf{k}, t)$ are the local plane waves obtained by a filter which localizes the wavefield in the propagating direction θ only. Making use of sets W and local plane-wave decomposition, we may decompose $u(\mathbf{x}, t)$ into a summation of local plane

waves in different directions consisting of terms of the form $\hat{u}(\theta, \mathbf{x}, t)$.

The proposed local plane-wave decomposition algorithm enjoys at least two unique features. The first feature is that it is accomplished very efficiently since no iteration is involved in the algorithm, and this is different from greedy-algorithm-based approaches, such as the matching pursuit algorithm (Wang and Wang, 2014) and the ALFT algorithm (Xu et al., 2005). The second is that the number of local plane waves is dramatically reduced since W is constructed from local maxima of $e(\theta)$. The angle resolution of this algorithm is mainly determined by the aperture X of the space window: the larger the space window is, the higher the angle resolution is, which is a manifestation of the uncertainty principle. However, a large space window may invalidate the local plane-wave assumption, which may generate smearing-effect artifacts in ADCIGs (Jin and McMechan, 2015). Some approaches are available to improve the angle resolution by imposing sparsity constraint and solving constrained optimization problems (Xu et al., 2011; Wang and Wang, 2014), but the resulting algorithm will increase the computational cost of the local plane-wave decomposition, making the overall decomposition less advantageous.

IMAGING CONDITIONS IN THE ANGLE DOMAIN

In the angle-domain imaging, we need to use local rectangular windows to partition the whole imaging domain so that local wavefronts are well approximated by local plane waves. In order to obtain ADCIGs from local plane-wave RTM algorithms, the imaging condition is applied to local plane waves and the imaging result is mapped to the angle domain. To simplify the presentation, we use the zero-lag cross-correlation-based imaging condition of

the extrapolated source and receiver wavefields. Therefore, the imaging result in the angle domain is computed by the following formulas:

$$R^{loc}(\mathbf{x}, \mathbf{x}_s, \theta, t) = \begin{cases} \hat{u}_s^{loc}(\alpha, \mathbf{x}, \mathbf{x}_s, t) \hat{u}_r^{loc}(\beta, \mathbf{x}, \mathbf{x}_s, t), & (\alpha - \beta) / 2 = \theta, \\ & \alpha \in W_s(t), \beta \in W_r(t) \\ 0, & else \end{cases} \quad (13)$$

$$I^{loc}(\mathbf{x}, \mathbf{x}_s, \theta) = \int R^{loc}(\mathbf{x}, \mathbf{x}_s, \theta, t) dt$$

where $\hat{u}_s^{loc}(\alpha, \mathbf{x}, \mathbf{x}_s, t)$ and $\hat{u}_r^{loc}(\beta, \mathbf{x}, \mathbf{x}_s, t)$ denote the local plane-wave decomposition of the source and receiver wavefields of the shot gather indexed by \mathbf{x}_s , respectively, and α and β are the propagating angles of the local plane waves. $W_s(t)$ and $W_r(t)$ denote the sets of propagating angles of the source and receiver wavefields in a local space window for given time t . In order to realize the imaging condition efficiently, we limit the number of elements in these two sets and only use significant local plane waves in the imaging condition. $R^{loc}(\mathbf{x}, \mathbf{x}_s, \theta, t)$ is the correlation result in the local space window for given t , and θ is the incident angle of the imaging result. By integrating $R^{loc}(\mathbf{x}, \mathbf{x}_s, \theta, t)$ with respect to time t , the ADCIGs of the shot gather indexed by \mathbf{x}_s are obtained. Since the imaging condition given by equation (13) is realized in the process of extrapolating the source and receiver wavefields in time, only slight changes are needed to accommodate the CWF construction and local plane-wave decomposition in existing RTM algorithms.

Equation (13) gives the approach to obtain ADCIGs in a local space window. By integrating these ADCIGs window by window, the final ADCIGs are obtained by using the following algorithm.

ALGORITHM: Imaging condition in the angle domain

For ($it = 0; it < nt; it++$)

{

For ($ix = 0; ix < nx; ix+ = X$)

{

For ($iz = 0; iz < nz; iz+ = Z$)

{

1. Get the Cauchy condition in the space window:

$\{(x, z) \mid |x - ix| < X/2, |z - iz| < Z/2\}$;

2. Construct the CWF from the Cauchy condition and equation (10);

3. Decompose the CWF into local plane waves with equation (11) and (12);

4. Apply the imaging condition defined in equation (13) to the local plane waves;

5. Obtain the local correlation result $R^{loc}(\mathbf{x}, \mathbf{x}_s, \theta, it)$;

}

}

6. Add $R^{loc}(\mathbf{x}, \mathbf{x}_s, \theta, it)$ to the final ADCIGs $I(\mathbf{x}, \mathbf{x}_s, \theta)$;

7. Get the wavefield indexed by $(it + 1)$;

}

Here nt , nx , and nz denote the number of sampling points of the wavefields along the t -, x - and z - direction, respectively; it , ix , and iz denote the indices of the time step and the space window, respectively. X and Z are the apertures of the local space window in the x - and z - direction, respectively. Although the CWF construction and local plane-wave decomposition are in the innermost loop of this algorithm, local space windows and FFT

algorithms are used to compute CWFs and significant local plane waves so that the computational cost of the resulting imaging condition is reasonable, yielding an efficient approach to obtain ADCIGs.

NUMERICAL EXAMPLES

We give some numerical examples to show how to obtain and apply CWFs in the angle-domain imaging. A local plane-wave RTM algorithm is used for all the following examples. First, we use a simple two-layer model to demonstrate applications of CWFs in terms of realizing imaging conditions. Then we use a layered model to demonstrate resolution effects of the space window on imaging results. Finally we use the Marmousi model to demonstrate the capability of the CWF-based imaging condition to obtain ADCIGs in complicated velocity models.

Illustrating the angle-domain imaging condition

A two-layer model is used to demonstrate the process of realizing the imaging condition proposed in this paper, which is shown in Figure 1. Figure 1(a) is a snapshot of the wavefield. Since the imaging condition is applied in a local space window, we need to decompose the wavefield into a sequence of local wavefields. Figure 1(b) is the Cauchy condition of a local wavefield shown in Figure 1(a). Using the Cauchy condition and equation (10), we can obtain the local CWF and its Fourier spectrum. Figure 1(c) shows the resulting local CWFs in the wavenumber domain and its energy distribution in the angle domain obtained

by equation (11). It is clear that the CWF in the wavenumber domain reveals polarization vectors accurately, which is useful for obtaining propagating angles of wavefronts. Figure 1(d) shows the local plane-wave decomposition result based on equation (12). Since the difference between the incident wave's propagation angle and the transmitted wave's is less than the angle resolution as shown in Figure 1(b), they are represented by the same local plane wave in Figure 1(d). Next we apply the correlation imaging condition to these local plane waves. Figure 1(e) shows the correlation result, where the left is the low-frequency noise arising from the RTM algorithm with incident angles being almost 90 degrees, and the right is the desired imaging result. Thus CWFs can also be used to attenuate the low-frequency noise of RTM by filtering out the imaging result due to larger incident angles. We obtain the final ADCIGs by integrating the correlation results in the t -direction.

A layered model

Figures 3 to 5 show some results of a layered model with the velocity model shown in Figure 2. Figures 3 and 4 show a single-shot imaging result and the slices of the ADCIG cube of the layered model. The source location of the shot gather used in Figures 3 and 4 is $s_x = 5$ km. The top subfigures in Figures 3 and 4 show the slices of the ADCIG cube at different depths. They give the illumination information of the subsurface in the angle domain. The bottom-right subfigures in Figures 3 and 4 are the slices of the ADCIG cube at different locations, while the bottom-left subfigures are the stacking results of ADCIGs, which form the final migration profile. Because this is based on a single-shot RTM and there are no multi-arrivals in the layered model, the energy distribution of the ADCIG cube

features one point for each position with a correct reflection angle. Figures 3 and 4 show that the ADCIGs obtained by our approach yield accurate reflection angles and the image energy is well concentrated around the correct angles. They also prove that the polarization vector obtained by the CWF is an ideal tool for obtaining accurate propagating angles of wavefronts. Another phenomenon shown in Figures 3 and 4 is that in comparison to shallow events deeper events have a narrower angle range with a denser sample rate, which has been explained by Tang et al. (2013). So the aliasing occurs easily when imaging the shallow layers, which degrades the quality of ADCIGs at shallow subsurface.

The difference between Figure 3 and Figure 4 is the aperture of the local space window. The aperture of the space window is 320 m for Figure 3, while it is 640 m for Figure 4. According to the sampling theory, a larger aperture improves resolution of propagating angles so that the angle resolution in Figure 4 is higher than that in Figure 3. But a large space window may invalidate the assumption of linear events, leading to migration artifacts and degrading the quality of final ADCIGs. Thus the choice of the window aperture has to be made by considering curvatures of wavefronts and complexity of velocity models.

Figure 5 shows the migration result of the layered model with multiple shots. The range of s_x in this figure is from 0 km to 10 km, and the sampling interval of s_x is 100 m. The window aperture used in this example is 640 m. The slices of the ADCIG cube shown in Figure 5 give the illumination information of the subsurface in the angle domain, which is important for survey design, AVA analysis, and interpretation. Moreover, curvatures of the events in ADCIGs also provide the information for migration velocity analysis. Because the true velocity model is used in this example, the events in ADCIGs are all flat.

The Marmousi model

Figures 6 to 8 show numerical results of the Marmousi model. Figures 6 and 7 show a single-shot migration result and the slices of the ADCIG cube. The source location of the shot gather used in Figures 6 and 7 is $s_x = 6$ km. Because the Marmousi model is more complex than the layered model, the wavefields of the Marmousi model are more complicated and multi-arrivals are abundant in the wavefields as shown in the slices of the ADCIG cube in Figures 6 and 7. Figures 6 and 7 also show that the proposed imaging condition is capable of processing complex wavefields and obtaining reliable illumination information of subsurface structures.

The difference between Figures 6 and 7 is the window aperture. The window aperture is 200 m in Figure 6, while it is 400 m in Figure 7. So it is clear that the angle resolution in Figure 7 is higher than that in Figure 6.

Figure 8 shows the imaging result of the Marmousi model with multiple shots. The range of s_x is from 3.6 km to 9.0 km. The window aperture used is 400 m. The slices of the ADCIG cube shown in Figure 8 prove that the ADCIG obtained by our approach yields the reliable illumination information of the subsurface with few artifacts. Since the migration profile is the stacking result of ADCIGs whose reflection angles are less than 60 degrees, the low-frequency noise of the usual RTM is attenuated in Figure 8. Therefore, CWFs and polarization vectors can also be used to attenuate the low-frequency noise of RTM and to improve the quality of migration result.

CONCLUSIONS AND DISCUSSIONS

In this paper, we proposed a new approach to obtain polarization vectors with Cauchy wavefields and a fast local plane-wave decomposition algorithm to implement the angle-domain imaging condition. The CWF is constructed from the Cauchy condition of the wave equation and contains only negative frequencies of the original wavefield. Polarization vectors are obtained from local CWFs in the wavenumber domain. Because the CWF is constructed efficiently by using the FFT algorithm, the computational cost for obtaining polarization vectors is low so that the imaging condition can be implemented efficiently.

The angle resolution of ADCIGs is mainly affected by the aperture of the local space window and curvatures of local wavefronts. According to the sampling theory, a large window aperture improves the angle resolution of ADCIGs. But if the wavefronts in the space window invalidate the assumption of linear events, the resolution of ADCIGs is also degraded. Thus the choice of window apertures has to be made according to curvatures of wavefronts and the complexity of the underlying velocity model.

ACKNOWLEDGEMENT

We gratefully acknowledge the financial support by the 973 project (2011 CB201002) and the great and special projects (2011ZX05005-005-008HZ and 2011ZX05006-002). Special thanks also go to Geophysics Research Institute of CNOOC Energy Technology and Services-Oilfield Technology Services Co. and SINOPEC Geophysics Research Institute (SGRI). Qian is supported by NSF grants 1222368 and 1522249.

REFERENCES

- Biondi, B, and W. Symes, 2004, Angle-domain common-image gathers for migration velocity analysis by wavefield-continuation imaging: *Geophysics*, **69**, 1283-1298.
- Cao, J., and R. S. Wu, 2009, Full-wave directional illumination analysis in the frequency domain: *Geophysics*, **74**, No. 4, S85-S93.
- De Bruin, C. G. M., C. P. A. Wapenaar, and A. J. Berkhout, 1990 Angle-dependent reflectivity by means of prestack migration: *Geophysics*, **55**, 1223-1234.
- Dickens, T. A., and G. A. Winbow, 2011, RTM angle gathers using Poynting vectors: 81st Annual International Meeting, SEG, Expanded Abstracts, 3109-3113.
- Fomel, S., 2004, Theory of 3-D angle gathers in wave-equation imaging: 74th Annual International Meeting, SEG, Expanded Abstracts, 1053-1056.
- Jin, H., and G. A. McMechan, 2015, Removing smearing-effect artifacts in angle-domain common-image gathers from reverse time migration: *Geophysics*, **80**, No. 3, U13-U24.
- Sava, P., and S. Fomel, 2003, Angle-domain common-image gathers by wavefield continuation methods: *Geophysics*, **68**, 1065-1074.
- Sava, P., and S. Fomel, 2006, Time-shift imaging condition in seismic migration: *Geophysics*, **71**, No. 6, S209-S217.
- Soubaras, R., 2003, Angle gathers for shot-record migration by local harmonic decomposition: 73rd Annual International Meeting, SEG, Expanded Abstracts, 889-892.

- Stolk, C., and W. Symes, 2004, Kinematic artifacts in prestack depth migration: *Geophysics*, **69**, 562-575.
- Tang, B., S. Xu, and Y. Zhang, 2013, 3D angle gathers with plane-wave reverse-time migration: *Geophysics*, **78**, No. 2, S117-S123.
- Vyas, M., D. Nichols, and E. Mobley E, 2011, Efficient RTM angle gathers using source directions: 81st Annual International Meeting, SEG, Expanded Abstracts, 3104-3108.
- Wang, X. W., and H. Z. Wang, 2014, A research of high-resolution plane-wave decomposition based on compressed sensing: *Chinese J. Geophysics*, **57**, 2946-2960.
- Wang, X. W., H. Z. Wang, and J. Qian, 2015, Generation of Angle Gathers by Decomposing the Initial Condition of Wave equation: 77th Conference and Exhibition, EAGE, Expanded Abstracts, TuP310.
- Wu, R. S., M. Luo, S. Chen, and X. Xie, 2004, Acquisition aperture correction in angle-domain and true-amplitude imaging for wave equation migration: 74th Annual International Meeting, SEG, Expanded Abstracts, 937-940.
- Xie, X. B., and R. S. Wu, 2002, Extracting angle domain information from migrated wavefield: 72nd Annual International Meeting, SEG, Expanded Abstracts, 1360-1363.
- Xie, X. B., and H. Yang, 2008, A full-wave equation based seismic illumination analysis method: 70th Conference and Exhibition, EAGE, Expanded Abstracts, P284.
- Xu, S., H. Chauris, G. Lambare, and M. Noble, 2001, Common-angle migration: A strategy for imaging complex media: *Geophysics*, **66**, 1877-1894.

- Xu, S., Y. Zhang, D. Pham, and G. Lambare, 2005, Antileakage Fourier transform for seismic data regularization: *Geophysics*, **70**, No. 4, V87-V95.
- Xu, S., Y. Zhang, and G. Lambare, 2010, Antileakage Fourier transform for seismic data regularization in higher dimensions: *Geophysics*, **75**, No. 6, WB113-WB120.
- Xu, S., Y. Zhang, and B. Tang, 2011, 3D angle gathers from reverse time migration: *Geophysics*, **76**, No. 2, S77-S92.
- Yan, R., and X. B. Xie, 2009, A new angle-domain imaging condition for prestack reverse-time migration: 79th Annual International Meeting, SEG, Expanded Abstracts, 2784-2788.
- Yoon, K., and K. Marfurt, 2006, Reverse-time migration using the Poynting vector: *Exploration Geophysics*, **37**, 102-107.
- Yoon, K., M. Guo, J. Cai, and B. Wang, 2011, 3D RTM angle gathers from source wave propagation direction and dip of reflector: 81st Annual International Meeting, SEG, Expanded Abstracts, 3136-3140.
- Zhang, Y., G. Zhang, and N. Bleistein, 2003, True amplitude wave equation migration arising from true amplitude one-way wave equations: *Inverse Problems*, **19**, 1113-1138.

LIST OF FIGURES

1 Realization of the imaging condition: (a) the snapshot of wavefields; (b) the local Cauchy condition in the space window shown in (a); (c) the CWFs in the wavenumber domain and its energy distribution in the angle domain; (d) the local plane-wave decomposition result; (e) the correlation result of local plane waves in the angle domain.

2 A layered velocity model used in Figures 3 to 5.

3 A single-shot imaging result of the layered model in the angle domain. The position of the source is $s_x = 5$ km. The top shows the slices of the ADCIG cube at different depths, which give the illumination information of the subsurface in the angle domain. The bottom-right subfigure shows the ADCIGs at different positions, while the bottom-left is the migration result. The aperture of the space window in this case is 320 m.

4 A single-shot imaging result of the layered model in the angle domain. The position of the source is $s_x = 5$ km. The top subfigure shows the slices of the ADCIG cube at different depths, which give the illumination information of the subsurface in the angle domain. The bottom-right subfigure shows the ADCIGs at different positions, while the bottom-left is the migration result. The aperture of the space window in this case is 640 m.

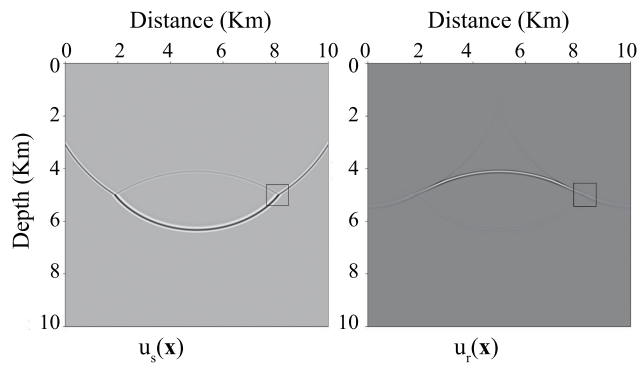
5 The imaging result of the layered model in the angle domain obtained with multiple shots. The range of s_x is from 0 km to 10 km, and the sampling interval of s_x is 100 m. The top subfigure shows the slices of the ADCIG cube at different depths, which yield the illumination information of the subsurface in the angle domain. The bottom-right subfigure is the ADCIGs at different positions, while the bottom-left is the migration result. The

aperture of the space window in this case is 640 m.

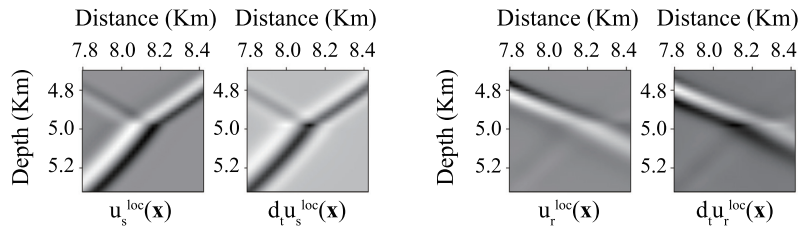
6 A single-shot imaging result of the Marmousi model in the angle domain. The position of the source is $s_x = 6$ km. (a) The slices of the ADCIG cube at different depths, which show the illumination information of the subsurface in the angle domain. (b) The ADCIGs at different positions. (c) The stacking result of ADCIGs. The aperture of the space window in this case is 200 m.

7 A single-shot imaging result of the Marmousi model in the angle domain. The position of the source is $s_x = 6$ km. (a) The slices of the ADCIG cube at different depths, which show the illumination information of the subsurface in the angle domain. (b) The ADCIGs at different positions. (c) The stacking result of ADCIGs. The aperture of the space window in this case is 400 m.

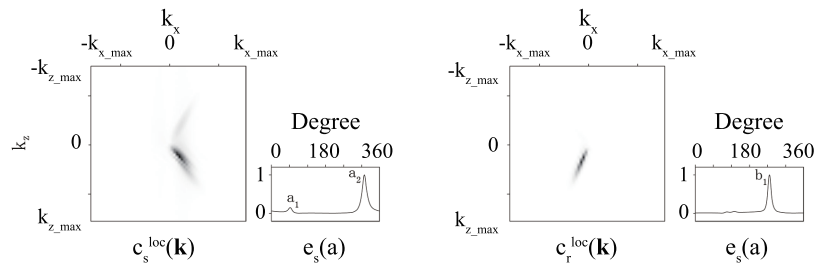
8 The imaging result of the Marmousi model in the angle domain obtained with multiple shots. The range of s_x is from 3.6 km to 9.0 km. (a) The slices of the ADCIG cube at different depths, which show the illumination information of the subsurface in the angle domain. (b) The ADCIGs at different positions. (c) The stacking result of ADCIGs. The aperture of the space window in this case is 400 m.



a)



b)



c)

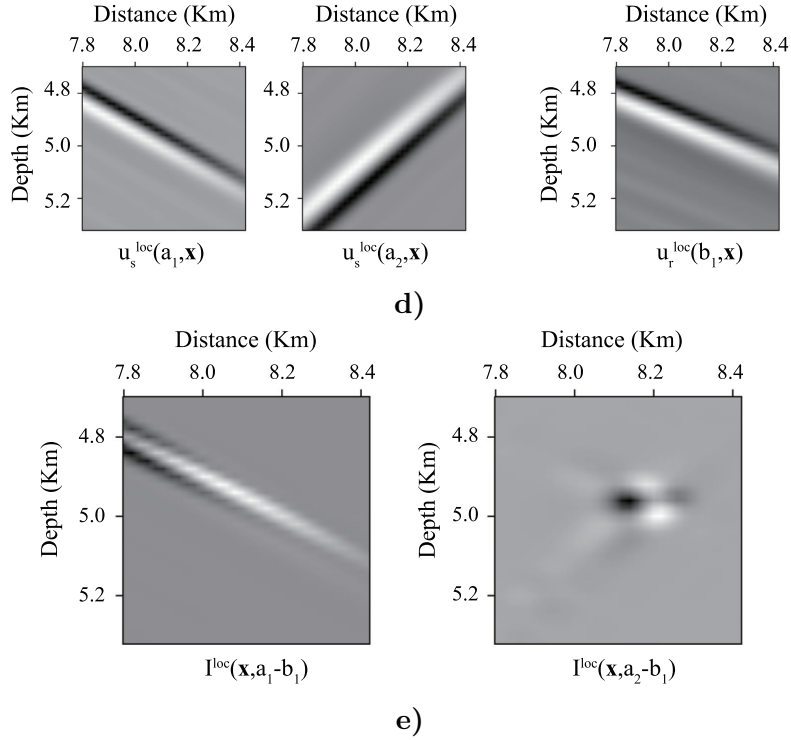


Figure 1: Realization of the imaging condition: (a) the snapshot of wavefields; (b) the local Cauchy condition in the space window shown in (a); (c) the CWFs in the wavenumber domain and its energy distribution in the angle domain; (d) the local plane-wave decomposition result; (e) the correlation result of local plane waves in the angle domain.

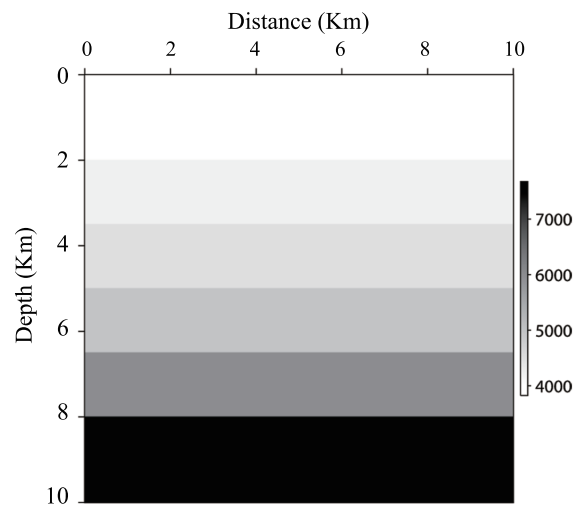


Figure 2: A layered velocity model used in Figures 3 to 5.

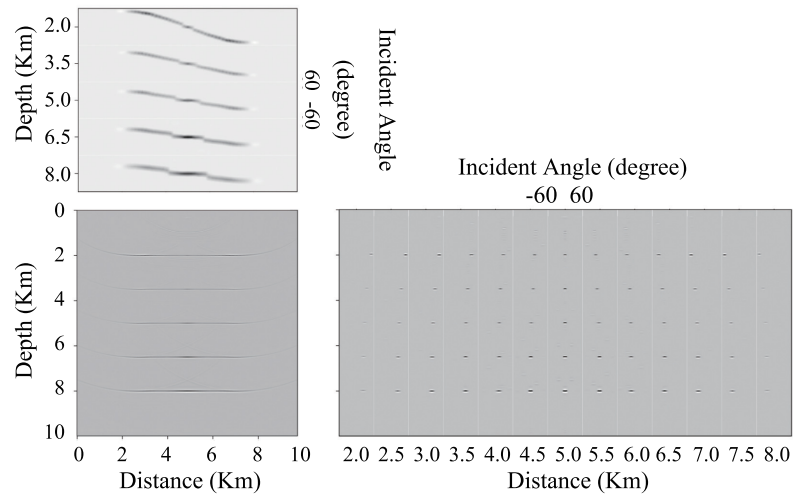


Figure 3: A single-shot imaging result of the layered model in the angle domain. The position of the source is $s_x = 5$ km. The top shows the slices of the ADCIG cube at different depths, which give the illumination information of the subsurface in the angle domain. The bottom-right subfigure shows the ADCIGs at different positions, while the bottom-left is the migration result. The aperture of the space window in this case is 320 m.

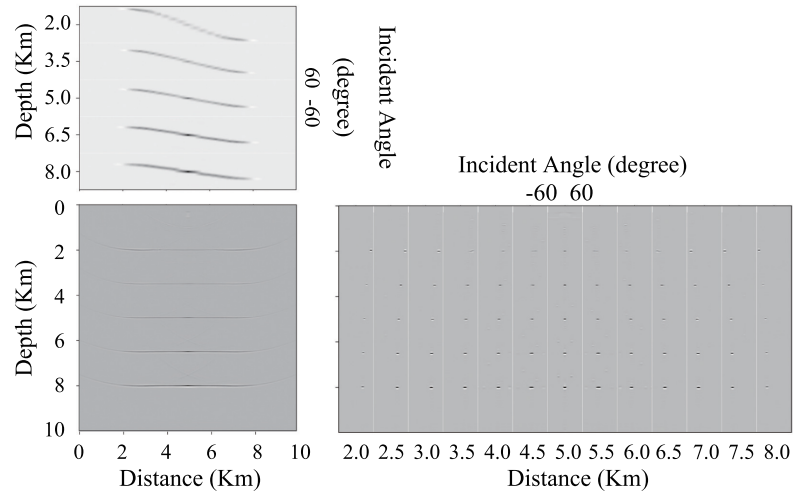


Figure 4: A single-shot imaging result of the layered model in the angle domain. The position of the source is $s_x = 5$ km. The top subfigure shows the slices of the ADCIG cube at different depths, which give the illumination information of the subsurface in the angle domain. The bottom-right subfigure shows the ADCIGs at different positions, while the bottom-left is the migration result. The aperture of the space window in this case is 640 m.

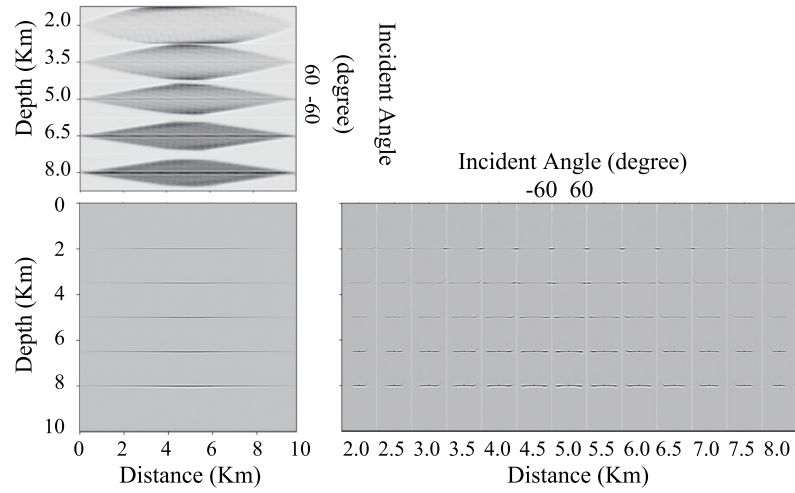
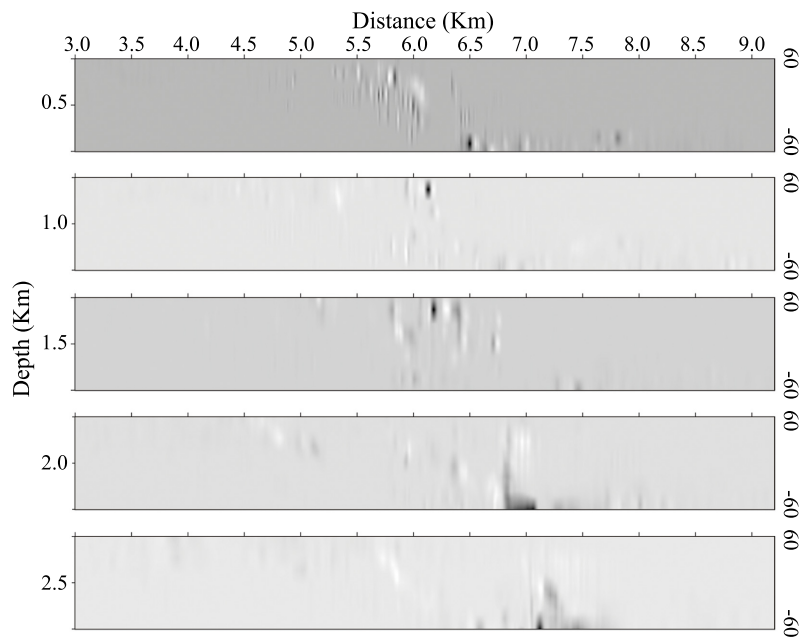
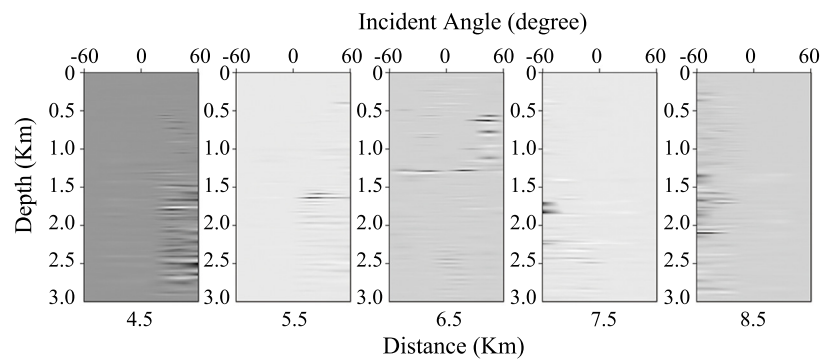


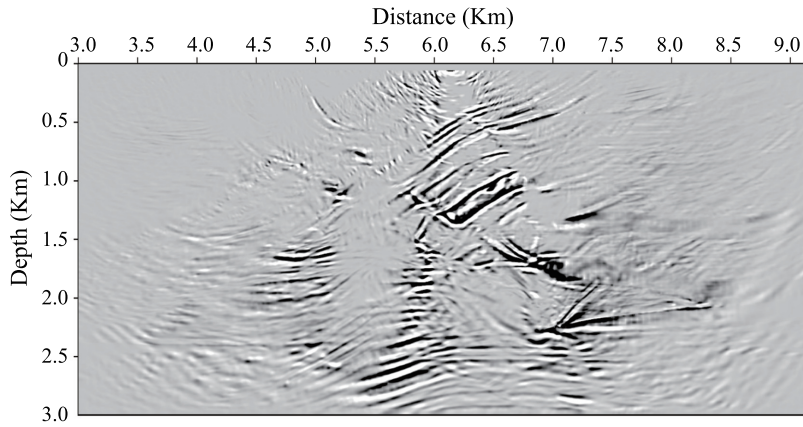
Figure 5: The imaging result of the layered model in the angle domain obtained with multiple shots. The range of s_x is from 0 km to 10 km, and the sampling interval of s_x is 100 m. The top subfigure shows the slices of the ADCIG cube at different depths, which yield the illumination information of the subsurface in the angle domain. The bottom-right subfigure is the ADCIGs at different positions, while the bottom-left is the migration result. The aperture of the space window in this case is 640 m.



a)

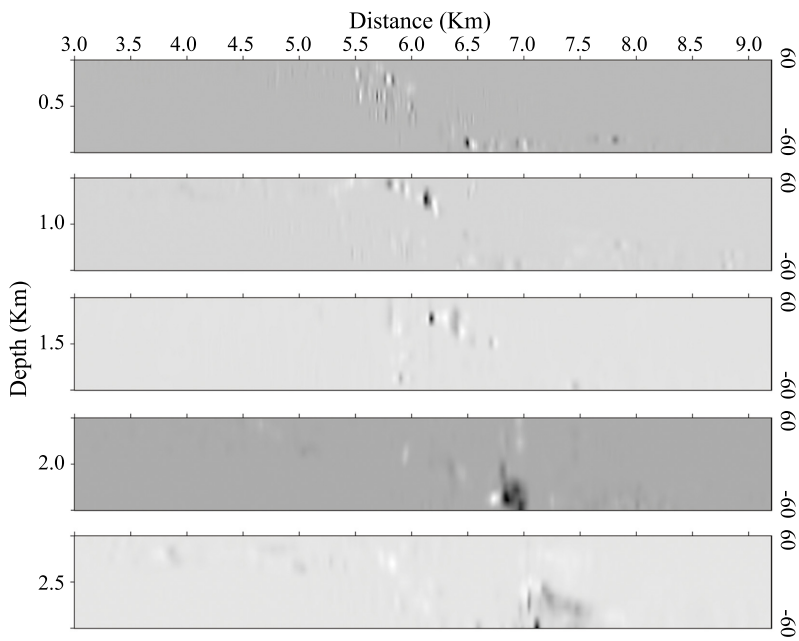


b)

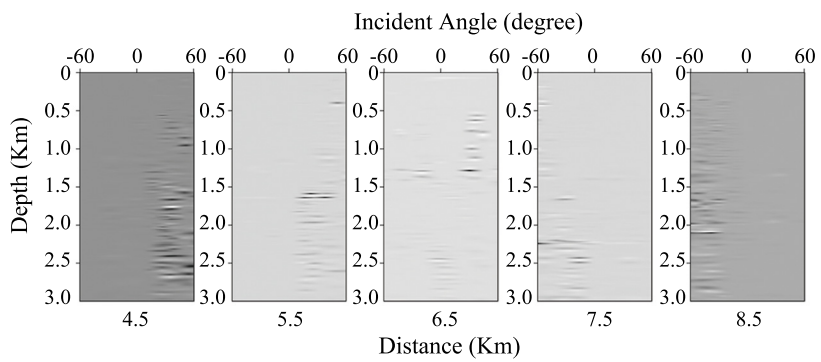


c)

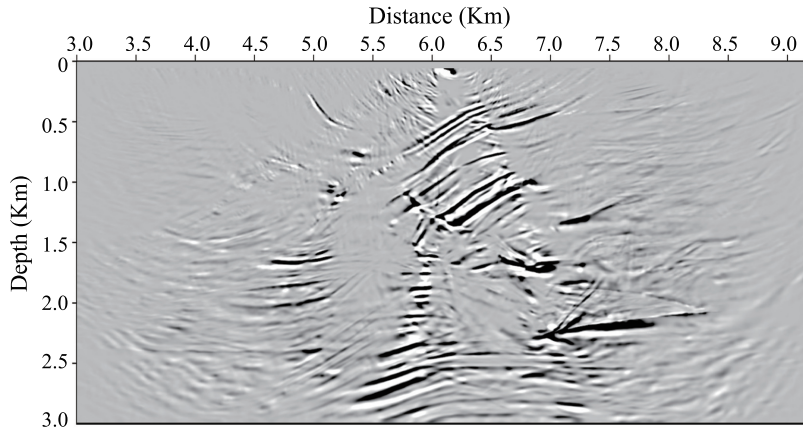
Figure 6: A single-shot imaging result of the Marmousi model in the angle domain. The position of the source is $s_x = 6$ km. (a) The slices of the ADCIG cube at different depths, which show the illumination information of the subsurface in the angle domain. (b) The ADCIGs at different positions. (c) The stacking result of ADCIGs. The aperture of the space window in this case is 200 m.



a)

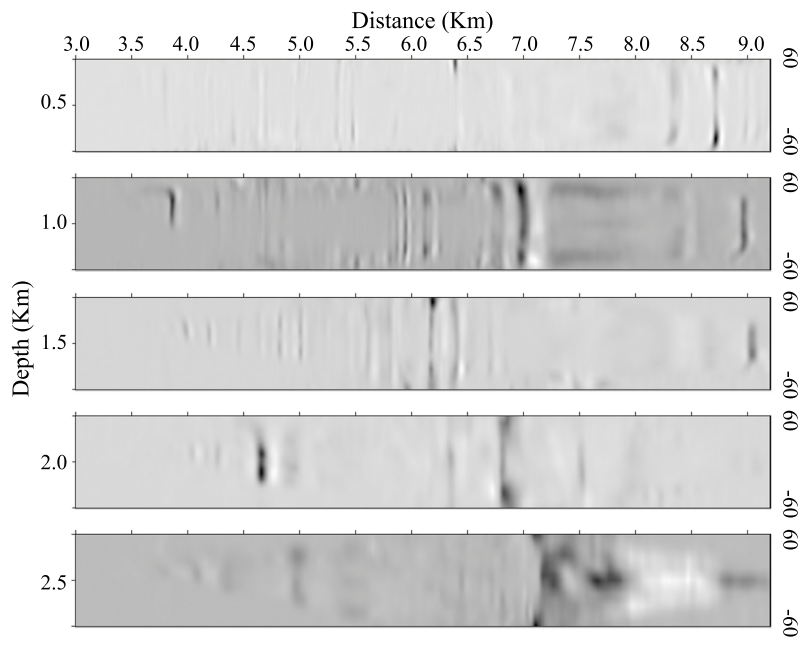


b)

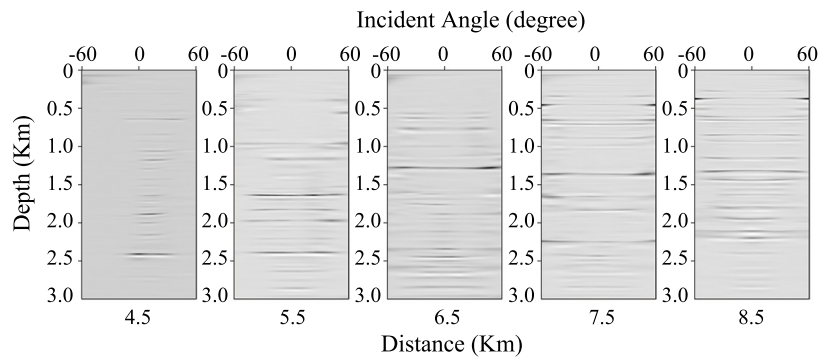


c)

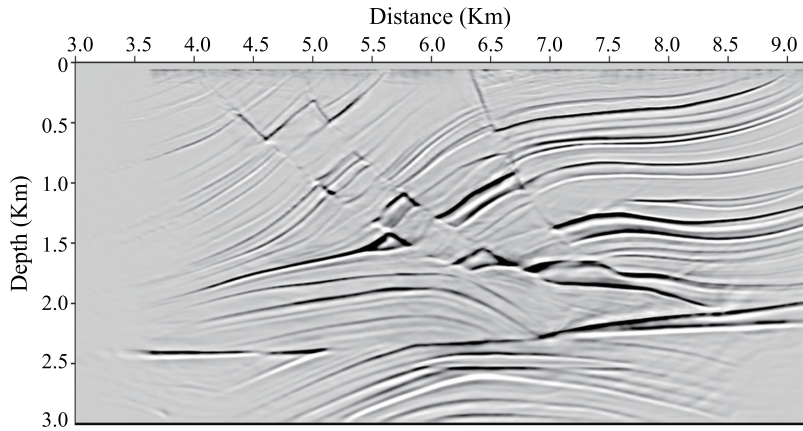
Figure 7: A single-shot imaging result of the Marmousi model in the angle domain. The position of the source is $s_x = 6$ km. (a) The slices of the ADCIG cube at different depths, which show the illumination information of the subsurface in the angle domain. (b) The ADCIGs at different positions. (c) The stacking result of ADCIGs. The aperture of the space window in this case is 400 m.



a)



b)



c)

Figure 8: The imaging result of the Marmousi model in the angle domain obtained with multiple shots. The range of s_x is from 3.6 km to 9.0 km. (a) The slices of the ADCIG cube at different depths, which show the illumination information of the subsurface in the angle domain. (b) The ADCIGs at different positions. (c) The stacking result of ADCIGs. The aperture of the space window in this case is 400 m.